Journal of Zhejiang University-SCIENCE A (Applied Physics & Engineering) 2025 26(6):512-524
www.jzus.zju.edu.cn; www.springer.com/journal/11582
E-mail: jzus_a@zju.edu.cn

Research Article

https://doi.org/10.1631/jzus.A2400260

Check for updates

Multi-directional wind energy harvesting based on the coupling effect between a piezoelectric beam and an elastic-supported sphere

Shun WENG[1], Liying WU[1], Lanbin ZHANG[2], Ke GAO[1], Junshu ZHANG[1], Zhiyue ZHANG[1], Huliang DAI[3]✉

[1]*School of Civil and Hydraulic Engineering, Huazhong University of Science and Technology, Wuhan 430074, China*
[2]*Faculty of Engineering, China University of Geosciences, Wuhan 430074, China*
[3]*School of Aerospace Engineering, Huazhong University of Science and Technology, Wuhan 430074, China*

Abstract: A new piezoelectric energy harvester is proposed which employs the coupling effect between a piezoelectric beam and an elastic-supported sphere to capture wind energy from multiple directions. As wind flows across the sphere, it induces vortical vibrations that transfer to the piezoelectric beam, converting wind energy into electricity. A nonlinear coupled dynamic theoretical model based on the Euler-Lagrange equation is developed to study the interactions between the sphere and beam vibrations. The vortex-induced force acting on the sphere is determined, and the dynamic model of the coupled system is validated through experiments. The results show that in order to reach convergence, at least four modes are required in the Galerkin discretization. Moreover, the output performance of the energy harvester strongly depends on the frequency ratio between the sphere and the piezoelectric beam. We find that at a frequency ratio of approximately 1.34, the harvester achieves a maximum average power of 190 μW at a wind speed of 3.90 m/s, with the lock-in region between 2.63 and 5.30 m/s. Subsequently, the impact of wind flow direction on the electrical performance of the energy harvester is investigated in a wind tunnel, by adjusting the angle between the harvester and incoming flows ranging from 0° to 360°. The findings indicate that the harvester maintains strong and consistent performance across variable wind flow directions and speeds. Particularly within the lock-in region, the output voltage fluctuations are below 5.5%, showcasing the robustness of the design. This result points to the potential utility of this novel harvester in complex environments. Our study also provides a theoretical basis for the development of small-scale offshore wind energy harvesting technologies.

Key words: Wind energy harvesting; Vortex-induced vibration (VIV); Piezoelectric effect; Lock-in region

1 Introduction

Civil infrastructure, such as buildings, bridges, and tunnels, inevitably encounters challenges from damage and aging. Structural health monitoring (SHM) is essential for the operation and maintenance of such structures, as it enables rapid detection of structural changes (Xie et al., 2020; Zhou et al., 2020). Recent advancements in wireless and low-power electronics have led to the adoption of structural health monitoring systems (SHMS). However, most wireless sensor network (WSN) nodes, powered by batteries or power lines, face issues such as the frequent need for battery replacement and complex wiring requirements. These challenges are especially significant in inaccessible areas, harsh conditions, and embedded environments, creating an urgent need for reliable power sources for WSN nodes (Wang et al., 2021a).

Energy harvesting involves converting energy from the environment into electrical power using various transduction technologies (Tao and Hu, 2016; Su et al., 2023). This process can charge the battery of a device or even eliminate the need for batteries. Micro-energy harvesting technologies, with output power levels ranging from microwatts to milliwatts, offer a practical solution for powering low-power electronic devices and developing self-sufficient energy. This technology can replace batteries and simplify maintenance in applications where battery replacement is inconvenient, costly, or hazardous.

✉ Huliang DAI, daihulianglx@hust.edu.cn
Shun WENG, https://orcid.org/0000-0001-9093-607X
Huliang DAI, https://orcid.org/0000-0003-0694-8866

Received June 5, 2024; Revision accepted Aug. 24, 2024;
Crosschecked Jan. 7, 2025; Online first Feb. 24, 2025

© Zhejiang University Press 2025

Among these technologies, piezoelectric energy harvesters stand out for their compatibility with microelectromechanical system (MEMS) devices, lack of need for an initial power supply, and their simple structure. Early research into piezoelectric energy harvesting focused on converting wasted mechanical vibrations into electricity. For instance, Xia et al. (2023) developed theoretical models to improve the performance and efficiency of electromechanical energy harvesters. Similarly, He et al. (2022), Wu and Xu (2022), and Machado et al. (2021) enhanced piezoelectric energy harvesters through innovative designs and optimization strategies. These advancements enabled devices to adapt to various environmental conditions, thereby increasing their energy harvesting efficiency.

Although piezoelectric energy harvesters that leverage base excitation are widely used (Huang SF et al., 2023), they often face limitations, such as the need for specific frequency tuning and limited energy capturing from random or broadband vibrations. In contrast, piezoelectric devices designed to capture energy from flow-induced vibrations offer distinct advantages, such as receptiveness to a broader range of frequencies and greater adaptability to varying environmental conditions (Wang et al., 2022; Huang DM et al., 2023). Vortex-induced vibration (VIV) is a phenomenon commonly observed in fluid flow. It induces periodic oscillations in structures, as driven by periodic vortical shedding forces. The lock-in phenomenon refers to the synchronization of a structure's vibration frequency with the frequency of the incoming flow, which occurs within a specific range of wind speeds known as the lock-in range. This synchronization enhances the energy conversion efficiency of the harvester, as it maximizes the interaction between the fluid flow and the vibrating structure. However, beyond this range, the efficiency of energy extraction diminishes due to the loss of this resonance condition. In energy harvesting research, the characteristics of VIV are often used to capture fluid energy through fluid flow. This vibration mode not only provides a mechanism for energy conversion but also introduces new challenges and opportunities for designing energy harvesters due to its unique nonlinear and multi-degree-of-freedom effects. VIV energy harvesters typically employ cylindrical shapes as bluff bodies (Jia et al., 2020; Wang et al., 2021b). Although the lock-in phenomenon of VIV allows for efficient energy conversion at specific wind speeds, this characteristic is only present within a small range of wind speeds. Outside this range, the vibrational mode of the cylinder changes, leading to a rapid decline in energy conversion efficiency. Therefore, to enhance the adaptability and efficiency of energy harvesters, researchers are currently trying to expand the lock-in range through various strategies, such as introducing nonlinear mechanisms (Zhang et al., 2017), increasing the number of structural degrees of freedom (Chen et al., 2023), or optimizing the structural design (Zhang et al., 2019).

In real environments, wind speed and direction are often unstable and variable, leading to reduced efficiency and wasted energy, which presents a significant challenge to traditional wind-induced vibration energy harvesters. Multi-directional energy harvesters are advantageous due to their adaptability to varying wind speeds and directions. Wang et al. (2020) summarized the current progress and challenges of converting wind and hydro energy into electrical power, and investigated several innovative devices and concepts. A typical method to improve energy harvesting performance is to induce multimodal vibrations by modifying cantilever beams (Wang et al., 2019; Hu et al., 2020). However, this method is limited by narrow wind speed ranges. In contrast, the 3D vortex structure inherent in sphere VIVs exhibits multiple vibrational modes, leading to a wider range of resonance winds and higher response amplitudes, which makes it more effective for capturing VIV energy.

Cylindrical structures typically exhibit VIVs with two main resonance modes, depending on the alignment of the vortex shedding frequency with the structure's natural frequency. However, this lock-in phenomenon occurs within a narrow wind speed range, outside of which energy conversion efficiency drops sharply. In contrast, the sphere exhibits a more complex 3D vortex structure, leading to multiple vibration modes and a broader range of resonant winds. This results in higher response amplitudes and a wider operational range for energy harvesting. The advantages of VIVs in the sphere include: a broader wind speed range for effective energy conversion, higher response amplitudes due to complex vortex shedding patterns, and the potential for multimodal vibrational energy harvesting in diverse flow conditions. Additionally, the inherent 3D vortex structure of spherical VIVs

presents new opportunities for designing energy harvesters that are adaptable to various environmental conditions. For instance, the asymmetrical wake behind a sphere, unlike the symmetrical wake of a cylinder, can lead to more stable and robust energy conversion. In summary, the VIVs of spheres offer significant potential for energy harvesting due to their unique fluid mechanical properties and wider operational capabilities. These advantages make spherical structures a promising avenue for developing the next generation of energy harvesting technologies.

However, the fluid dynamics of sphere VIVs are complex, and researchers are still investigating their underlying mechanisms. Govardhan and Williamson (1997), Williamson and Govardhan (1997), and Rajamuni et al. (2020) each identified four VIV modes in tethered spheres that were immersed in fluid. These are resonance modes characterized by high vibration amplitudes and frequencies that closely match the natural frequencies. Studies have also focused on the dynamic response of elastically mounted spheres in uniform flow. For instance, Behara and Sotiropoulos (2016) and Negri et al. (2018) explored multidirectional VIV modes in elastically tethered spheres. Rajamuni et al. (2019) further compared the multi-degree-of-freedom dynamic characteristics of an elastically tethered sphere. Specifically, they examined the dynamic response, force coefficients, and wake structures. Also, advances in computing power have made numerical simulation a viable method for studying VIVs. Accordingly, Raza et al. (2020) investigated the VIVs of the sphere at moderate Reynolds numbers, and Rajamuni et al. (2018) incorporated transverse rotation into an analysis model for the sphere. They found that rotation reduced the oscillation amplitude and shrunk the lock-in region, and the VIV response was related to the Reynolds number.

In this study, we develop a multi-directional energy harvester based on the coupling effect between the VIVs of a sphere and a piezoelectric beam. First, a theoretical model is established and validated through experiments. Second, the impact of the ratio between the natural frequency of the sphere and the piezoelectric beam on the mechanical response and electrical performance is investigated. Finally, the effect of wind flow direction on the energy harvesting performance is examined.

2 Modeling and principle

We present an energy harvesting system that utilizes sphere VIVs to drive piezoelectric beams for electricity generation, as depicted in Fig. 1. The proposed device can harvest multi-directional wind energy above the surface of the water body, and supply power to surrounding sensors. The energy harvester is simplified to the computational model depicted in Fig. 2. In Fig. 2, l_1 and l_2 are the lengths of spring 1 and spring 2, respectively; l_1' and l_2' are the initial elongations of spring 1 and spring 2, respectively; k_1 and k_2 are the stiffnesses of spring 1 and spring 2, respectively; L_p and L_b are the lengths of the piezoelectric layer and the beam, respectively; W_p and W_b are the widths of the piezoelectric layer and the beam, respectively; t_p and t_b are the thicknesses of the piezoelectric layer and the beam, respectively; t_0 is the distance from neutral layer to bottom of piezoelectric beam; t_1 and t_2 are the distances from neutral layer to top of the

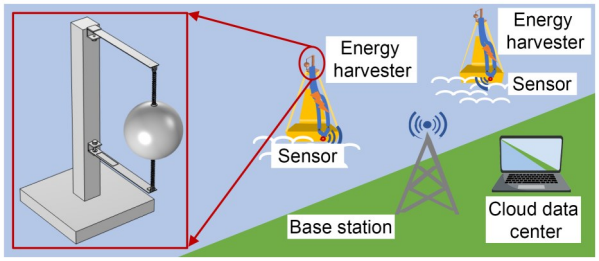

Fig. 1 Proposed energy harvester attached to a buoy on a body of water

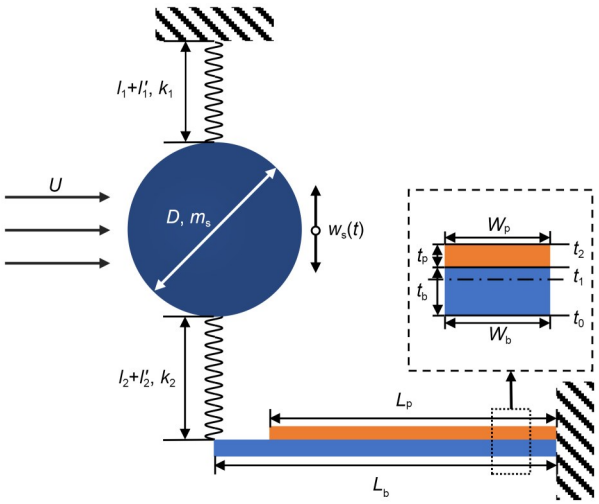

Fig. 2 Simplified computational model of the proposed energy harvester

metal layer and the piezoelectric layer, respectively. The sphere is connected via spring 1 to the fixed supports above, and via spring 2 to the flexible cantilever beam below. The flexible cantilever beam is composed of a metal layer and a piezoelectric layer, making it a piezoelectric beam. The material of metal layer is aluminium. The material of piezoelectric layer is macro-fiber composite (MFC). The thicknesses of both the piezoelectric layer and the beam are negligible, so shear deformation and rotational inertia can be ignored. This system generates energy through the bending of the beam induced by the sphere's VIVs.

The dynamics of VIV of an elastically mounted sphere is simplified to the case of a linear oscillator, with a detailed derivation provided in Section S1 of the electronic supplementary materials (ESM). The term $F_{\mathrm{VIV}}(t)$ stands for the vortex-induced force exerted by the wind flow on the sphere. The model of the coupled effect between the piezoelectric beam and sphere is derived as follows:

$$m_{\mathrm{s}}\ddot{w}_{\mathrm{s}}(t)+c\dot{w}_{\mathrm{s}}(t)+(k_1+k_2)w_{\mathrm{s}}(t)=F_{\mathrm{VIV}}(t), \quad (1)$$

$$F_{\mathrm{VIV}}(t)=\frac{\pi C_{\mathrm{L}}\rho_{\mathrm{a}}D^2U^2}{16}q(t)-\frac{\pi C_{\mathrm{D}}\rho_{\mathrm{a}}D^2U}{8}\dot{w}_{\mathrm{s}}(t), \quad (2)$$

$$\ddot{q}(t)+\lambda\omega_{\mathrm{s}}(q^2(t)-1)\dot{q}(t)+\omega_{\mathrm{s}}^2q(t)=\frac{A}{D}\ddot{w}_{\mathrm{s}}(t), \quad (3)$$

where $w_{\mathrm{s}}(t)$, $\dot{w}_{\mathrm{s}}(t)$, and $\ddot{w}_{\mathrm{s}}(t)$ are the displacement, velocity, and acceleration of the sphere on the vertical direction, respectively; t is the time; m_{s} and c are the total mass of the sphere and springs and the structural damping, respectively; C_{L} and C_{D} denote the steady mean lift coefficient and drag coefficient, respectively; U denotes the wind speed; D represents the diameter of the sphere; ρ_{a} denotes the density of the air; $q(t)$ is the fluid-structure coupling term; A represents a constant of the van der Pol wake oscillator model (A=23); λ is a constant describing vortex street fluctuation (λ=0.1); ω_{s} denotes the vortex shedding frequency. Both λ and A are determined from experimental results according to Facchinetti et al. (2004).

Facchinetti et al. (2004) provided the theoretical foundation for understanding vortex-induced forces and wake oscillator behavior. Eqs. (1) and (2) calculate the vortex-induced force, accounting for the periodicity of the vortex shedding and the fluid pressure distribution on the sphere's surface. Eq. (3) describes the dynamic behavior of the wake oscillator under vortex-induced forces, incorporating the mass, damping characteristics, and torque induced by the vortex force. x denotes the distance from any location on the beam to the clamped end. Assuming the vibrational response of the piezoelectric beam is $w_{\mathrm{b}}(x, t)$, it can be expressed as the product of the beam mode function matrix and the generalized time coordinate matrix, given by $w_{\mathrm{b}}(x,t)=\sum_{i=1}^{n}\Phi_i(x)Y_i(t)$, where i is the number of the modes. $Y_i(t)$ is the modal coordinates of the displacement and $\Phi_i(x)$ is the mode shapes of the piezoelectric beam. The calculation method using the Galerkin method follows the approach detailed by Dai et al. (2014).

The vortex-induced force is transmitted to the piezoelectric beam through spring 2. According to Hooke's law, the spring force is given by:

$$F_{\mathrm{sp}}=k_2(l_2'+w_{\mathrm{s}}(t)-w_{\mathrm{b}}(L_{\mathrm{b}},t)), \quad (4)$$

where $w_{\mathrm{b}}(L_{\mathrm{b}}, t)$ denotes the end displacement of the piezoelectric beam.

According to the Galerkin discretization method, the reduced-order model of the couple model is derived as follows:

$$\ddot{Y}_i(t)+2\varsigma_i\omega_i\dot{Y}_i(t)+\omega_i^2Y_i(t)-\theta_iV(t)=F_{\mathrm{sp}}, \quad (5)$$

where ς_i and ω_i denotes the aerodynamic damping and natural frequency of the sphere, respectively; θ_i is the electromechanical coupling coefficient; $V(t)$ denotes the voltage. According to Ohm's law, the voltage $V(t)$ across a resistor is directly proportional to the current passing through it. By also considering the definition of current, the following equation can be obtained:

$$C_{\mathrm{P}}\dot{V}(t)+\frac{V(t)}{R}+\sum_{i=1}^{n}\theta_i\dot{Y}_i(t)=0, \quad (6)$$

where C_{p} and R denote the capacitance and load resistance of the piezoelectric beam, respectively.

3 Validation of the theoretical model

3.1 Determination of the vortex-induced force

Fig. 3 illustrates a schematic of VIV of a bluff body sphere, with Fig. 3a depicting the variation of lift and drag force coefficients (C_{L} and C_{D}) with reduced

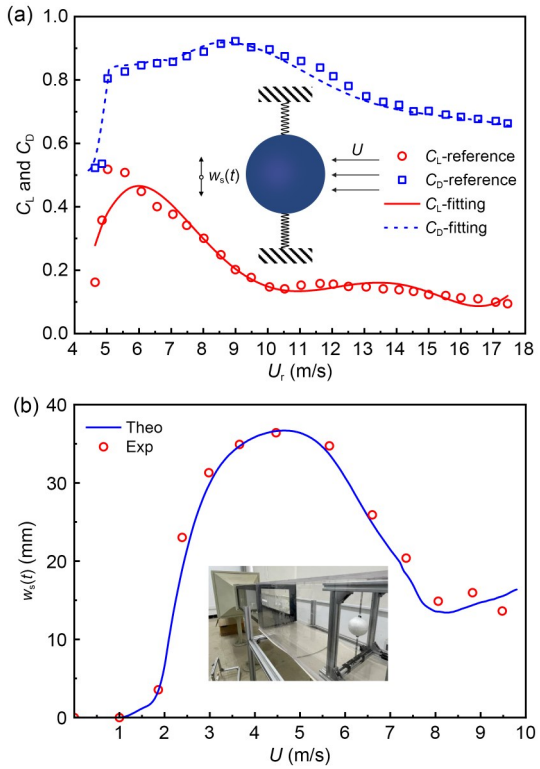

Fig. 3 (a) Schematic model of the elastically mounted sphere and variations of lift and drag force coefficients (C_L and C_D) with reduced velocity U_r; (b) experimental setup and the theoretical (Theo) and experimental (Exp) displacements of the sphere under different wind speeds

velocity U_r, as reported by Sareen et al. (2018). At the onset of the lock-in region, C_L initially increases and then continuously decreases. During this reduction, small amplitude oscillations occur. Beyond U_r=10 m/s, C_L almost remains constant. The C_D also increases sharply when the lock-in region begins. The accuracy of the theoretical model is validated through wind tunnel experiments, using the setup detailed in Section S2 of the ESM.

Fig. 3b shows the variation of the sphere's vibrational amplitude with wind speed. When U is below 4.47 m/s, a gradual increase in amplitude ensues, reaching a peak at U=4.47 m/s. In the subsequent range of 4.47 to 8.06 m/s, the amplitude gradually decreases. A noteworthy shift occurs in the range where U exceeds 8.06 m/s, which is characterized by a slight rebound. The comparative analysis of the experimental and numerical results shows consistent maximum and minimum amplitudes under the same velocity conditions. However, a slight discrepancy emerges when the wind speed exceeds 8.06 m/s. Numerical simulations suggest an increase in amplitude, indicative of a transition from a large-amplitude, stable vibration mode of self-locking characteristics to a more complex fluid-structure interaction mode. In contrast, the experimental results initially show an increase in amplitude, followed by a slight decrease. This variation in amplitude is attributed to the fluid flow characteristics observed during the experiment, where the 3D nature of the wake generates a significant vibration component. Consequently, the restraining springs apply both downstream and cross-flow constraints, causing a deviation in the sphere's vibration mode from the anticipated cross-flow mode.

Within the self-locking region, the sphere primarily exhibits vertical vibrations due to the periodic force provided by the spring. These vibrations are the most effective for energy harvesting as they directly cause the deformation of the piezoelectric beam. When the wind speed deviates from the self-locking region, the sphere's horizontal vibration amplitude increases while its vertical vibration amplitude decreases. Although the sphere moves laterally under these conditions, its contribution to the piezoelectric beam's deformation is minimal, limiting its impact on power generation efficiency. At higher wind speeds, the sphere stabilizes at the equilibrium position due to the combined effects of the wind and spring forces, further reducing the vibration amplitude. Consequently, both the deformation of the piezoelectric beam and its power generation capacity are significantly reduced. This study focuses on optimizing vertical vibrations within the self-locking region, as this mechanism provides the most effective energy conversion for VIVs. Although the sphere also exhibits horizontal vibrations under other wind speed conditions, these contribute less to energy harvesting and are therefore not considered as a primary factor.

3.2 Experimental validation

To validate the feasibility of the proposed device and theoretical model, a series of wind tunnel experiments are conducted. The sample and experimental setup are shown in Figs. 4a and 4b, while detailed geometric and physical characteristics of the sample are listed in Table 1. Details of the experimental setup and the fabrication of the proposed device are provided in Section S2.

Looking at Fig. 4c, the curve depicting the variation of peak open-circuit voltage (V_{oc}) with wind speed (as predicted using the Galerkin discretization method)

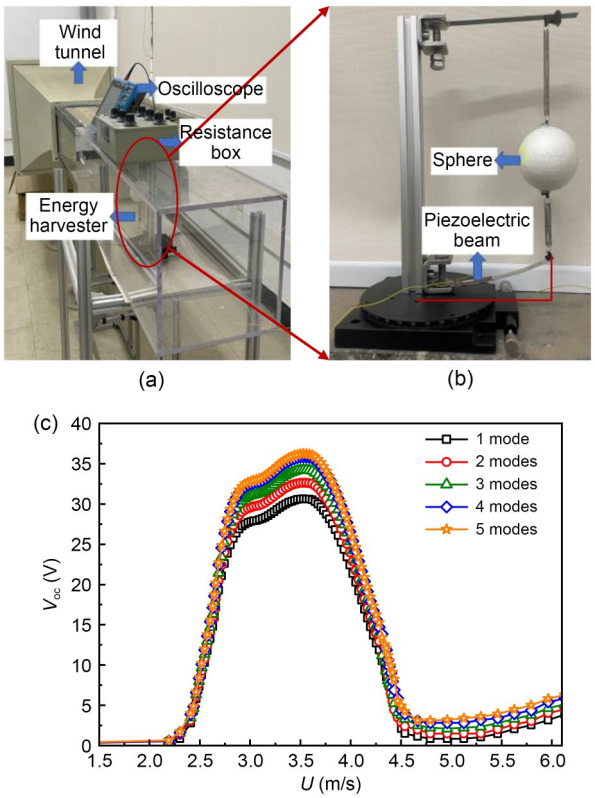

Fig. 4 (a) Experimental setup of the proposed device; (b) photograph of the sample; (c) variation of peak open-circuit voltage of the device with wind speed and number of modes

Table 1 Geometric and physical properties of the device components

Component	Parameter	Value
Sphere	Mass, m_s (g)	2.02
	Diameter, D (mm)	56.8
Spring	Stiffness of spring 1, k_1 (N/m)	11.9
	Stiffness of spring 2, k_2 (N/m)	11.9
Beam	Length, L_b (mm)	120
	Width, W_b (mm)	10
	Thickness, t_b (mm)	0.6
	Mass density, ρ_b (kg/m^3)	2700
	Young's modulus, E_b (GPa)	70
Piezoelectric layer	Length, L_p (mm)	28
	Width, W_p (mm)	7
	Thickness, t_p (mm)	0.3
	Mass density, ρ_p (kg/m^3)	7700
	Young's modulus, E_p (GPa)	30.336
	Strain coefficient, d_{31} (pm/V)	−190
	Permittivity at constant strain, ε_{33} (nF/m)	13.28
	Capacitance, C_p (nF)	15.1

reveals the significant influence of mode number on prediction accuracy. With only one or two modes, the predicted voltage values do not converge, resulting in the underestimation of both voltage and power output. This indicates that models with one or two modes cannot fully capture the complexity of the power generation. Increasing the number of modes to three improves prediction accuracy, but it still does not achieve the desired level of convergence. However, including four or five modes results in consistent and nearly identical predicted voltage and power values, indicating better convergence. This finding suggests that at least four modes are needed in the Galerkin discretization to ensure the accuracy of the voltage prediction. While increasing the number of modes can enhance the prediction accuracy, it is also essential to balance this accuracy with computational cost. Therefore, selecting the appropriate number of modes is crucial for efficient and accurate predictions, and as such should be determined based on the specific application scenario and precision requirements.

The vibration amplitudes of the spherical bluff body (w_s) and the beam end (w_b) for various wind speeds are shown in Figs. 5a and 5b. We can observe different phenomena here as compared to Fig. 3b. The lock-in region for the model in Fig. 5a is 0.64–6.04 m/s, while in Fig. 3 it is 1.63–8.06 m/s, demonstrating that the designed structure effectively converts fluid flow energy, even at low speeds. Notably, at U=3.2 m/s the amplitude exceeds the maximum amplitude of 38 mm observed in the model in Fig. 3b. This sudden increase is due to the support design and the elasticity of the underlying cantilever beam. Looking closer at Fig. 5b, it appears that the structure reaches resonance at the wind speed of 3.2 m/s, significantly increasing the amplitude and enhancing the wind energy conversion efficiency. This design advantage allows the model to achieve a high energy output even at relatively low wind speeds. Moreover, adjusting the stiffness of the piezoelectric beam enables tuning of the structure's natural frequency, thereby enhancing the output performance at different wind speeds.

The open-circuit voltage of the designed device is shown in Fig. 5c. The electrical response of the structure is consistent with the vibration characteristics depicted in Figs. 5a and 5b. As we can see, the lock-in region is approximately 2.63–5.30 m/s. As the vibration amplitude increases, the charge generated

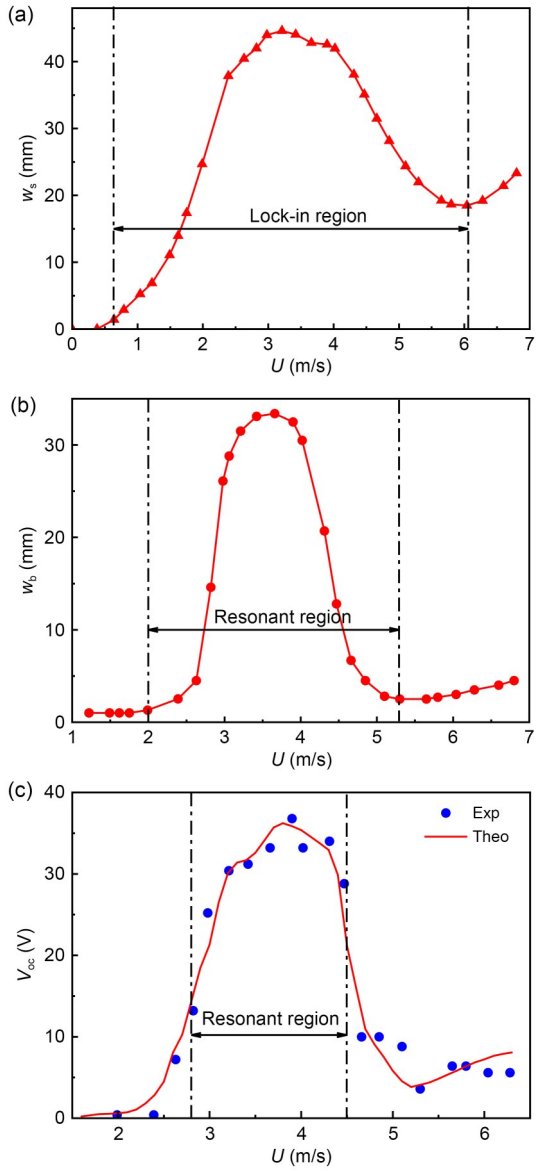

Fig. 5 (a) Variation of the vibration amplitude of the sphere with wind speed; (b) variation of the end displacement of the piezoelectric beam with wind speed; (c) variation of the peak open-circuit voltage with wind speed

by the piezoelectric effect also increases, resulting in a higher output voltage. Outside this region, the output voltage rapidly decreases. At the critical wind speed of 2.63 m/s, the open-circuit voltage peaks at 36.8 V (experimentally) and 36.2 V (theoretically). The close match between the experimental and theoretical results further demonstrates the accuracy of the proposed model. The open-circuit voltage sharply declines to its lowest point at U=5.30 m/s. When the wind speed exceeds 5.30 m/s, the sphere oscillates laterally, causing the cantilever beam to bend due to spring expansion and contraction, which leads to a rebound in the open-circuit voltage.

To investigate the optimal load resistance R, the variations of root mean square (RMS) voltage V_{rms} and average output power P_{avg} with load resistance are shown in Fig. S1 of the ESM. It is known that structural resonance significantly impacts energy harvesting efficiency (Wu et al., 2021). Thus, three wind speeds were analyzed: the wind speed corresponding to the maximum amplitude (U=3.90 m/s), the initial wind speed of the lock-in region (U=2.63 m/s), and the wind speed at the end of the lock-in region (U=4.47 m/s). The variations of V_{rms} and P_{avg} with load resistance at the three representative wind speeds are shown in Figs. S1a and S1b. As shown in Fig. S1a, the V_{rms} increases with increasing load resistance. This is due to the power generation characteristics of piezoelectric elements: in the absence of an external load, the charges generated by the piezoelectric effect accumulate and increase the electric field strength until the balance is reached. Accordingly, the ability to generate additional charges is reduced. Introducing an external load resistor provides a discharge path, enabling the piezoelectric material to continue generating charges.

However, the P_{avg} does not increase monotonically with R. As the R increases from 0.05 to 1.00 MΩ, and then to 10 MΩ, P_{avg} initially increases and then decreases. This occurs because, in the energy harvesting system, the energy transfer efficiency is maximized when the R matches the system's dynamic impedance. If the R is too low, significant energy is lost within the system; if it is too high, the system cannot efficiently transfer energy to the load. The variations in P_{avg} suggest the existence of an optimal load resistance that maximizes the P_{avg}. Fig. S1 shows that the P_{avg} reaches a peak at a load resistance of 1.00 MΩ. At this optimal load resistance, the energy conversion efficiency is the highest and the maximum power output is provided.

4 Output performance results

4.1 Influence of natural frequencies on output performance

To optimize the mechanical and electrical performance, the natural frequencies of both the sphere

system and the piezoelectric beam must be tuned. This relationship can be described by a dimensionless frequency (η), defined as the ratio of the natural frequency of the sphere system (f_s) to that of the piezoelectric beam (f_b), which is expressed as $\eta=f_s/f_b$. To elucidate the relationship, we vary the diameters of the sphere (D) from 50 to 80 mm; meanwhile, we vary the stiffness of the springs (k_1 and k_2) from 6 to 16 N/m, respectively. The resulting calculations show the relationships between sphere diameter, spring stiffness, and natural frequency, as shown in Fig. S2 of the ESM. Fig. S2a shows that the f_s increases with increasing spring stiffness, which also indicates that larger sphere diameters strongly influence the natural frequency. Fig. S2b illustrates the relationship between the piezoelectric beam length (L_b) and its natural frequency (f_b) for different beam widths (W_b). Specifically, it shows that the f_b decreases with increasing L_b, indicating a reduced stiffness of the piezoelectric beam as length increases. Similarly, increasing the beam width raises its natural frequency.

Fig. S2c shows the influence curve of dimensionless frequency η on the VIV amplitude w_s of the sphere at a wind speed of 3.90 m/s. The natural frequency of the sphere spring system depends on its diameter (D) and the stiffness of the tension springs. Larger sphere diameter and lower spring stiffness tend to reduce the structure's natural frequency. The natural frequency of the piezoelectric beam is influenced by its dimensions (length and width). Increasing the beam length typically lowers its natural frequency, whereas increasing the width raises it. At η=0, the piezoelectric beam is treated as a rigid support with infinite stiffness, resulting in a low vibration amplitude for the sphere. This indicates that with rigid support, the sphere's response to wind excitation is constrained.

As η increases, the sphere's amplitude first increases slowly and then decreases rapidly. This trend suggests an optimal dimensionless frequency at which the sphere's VIV response is maximized. At η=1.34, the sphere's amplitude peaks at 43.8 mm. This is because the matching of f_s and f_b leads to resonance, which maximizes the energy transfer efficiency. It also indicates that the coupling effect between the structure's natural frequency and the sphere's VIV characteristics is optimized at η=1.34. When η exceeds 1.5, the sphere's amplitude decreases rapidly. This is due to the equivalent stiffness of the piezoelectric beam being too low to maintain the sphere's vibration mode, resulting in reduced energy transfer efficiency.

In Fig. S2d, we present the relationship between η and P_{avg} at U=3.90 m/s. As one can observe, the P_{avg} (190 μW) reaches a peak at η=1.34. This suggests that when the natural frequency of the sphere system is 1.34 times that of the piezoelectric beam, the energy transfer efficiency of the system is the highest, reflecting optimal resonance. The lock-in region for the spherical bluff body helps maintain the resonant mode. Thus, by setting a fixed vibration frequency, the system can operate at optimal performance. Fig. S2 indicates that resonance is essential to our proposed piezoelectric energy harvesting system. By tuning the natural frequencies of both the sphere system and the piezoelectric beam, the maximum energy harvesting efficiency can be achieved.

Fig. S3 of the ESM shows the fast Fourier transform (FFT) of the output power signal at U=3.90 m/s for various dimensionless frequencies η. This plot illustrates the effect of frequency ratio on electrical performance by presenting the FFT of the output power signal, which indicates the resonant frequency of the piezoelectric beam. In Fig. S3a, when the wind speed is 3.90 m/s and the dimensionless frequency is 0.569, the average output power of the energy harvester reaches a peak of 11.11 Hz. This indicates that at this frequency ratio, the harvester's vibration frequency aligns with the vortex shedding frequency caused by the wind, leading to efficient energy conversion. At other frequencies, the output power fluctuates less, suggesting that these frequencies do not synchronize with the fluid-induced vibration, resulting in reduced energy conversion efficiency. Looking at Fig. S3b, with a wind speed of 3.90 m/s and a dimensionless frequency of 1.34, the average output power of the energy harvester reaches a peak at 14.22 Hz. At this frequency ratio, the harvester synchronizes with the vortex shedding frequency at a higher range, achieving efficient energy conversion.

Comparing Figs. S3a and S3b, it is evident that the frequency ratio affects the resonant frequency of the device. According to Govardhan and Williamson (1997), VIVs of a sphere exhibit a self-locking effect. Specifically, within a certain frequency range, the vibration amplitude of the sphere significantly increases, leading to the resonance. However, when the

excitation frequency deviates from this range, the vibration amplitude of the sphere sharply decreases, resulting in almost no vibration. Near the resonant frequency, energy transfer efficiency is maximized, enabling vibrational energy effectively transfer to the cantilever beam and yielding significant electrical output. Conversely, at non-resonant frequencies, reduced vibration amplitude decreases the energy transfer efficiency, significantly reducing the cantilever beam's deformation and power generation capability. This explains why only one significant resonance peak is observed in the FFT spectrum.

To summarize the effect of frequency ratio on the resonant frequency, Figs. 6a and 6b show the change in vibration frequency (f) with wind speed as the dimensionless frequency varies. Inspecting Figs. 6a and 6b, we can see that at a constant dimensionless frequency η, the relationship between vibration frequency and wind speed is approximately linear. Additionally, the smaller the dimensionless frequency η, the lower the wind speed required to initiate vibration. Figs. 6c and 6d depict the change in the average output power P_{avg} with wind speed under different dimensionless frequencies. Clearly, as the dimensionless frequency η increases, the lock-in region shifts rightward, causing the peak output power to shift accordingly. This occurs because a larger dimensionless frequency η corresponds to a higher natural frequency of the structure, which requires a higher flow rate to achieve the same excitation frequency.

Comparing Figs. 6c and 6d reveals that when η ranges from 0.971 to 1.473, the output power is relatively high, indicating optimal energy harvesting efficiency within this range. The coupling vibrations between the piezoelectric beam and the sphere system influence each other. This interaction optimizes vibration patterns and energy transfer at specific dimensionless frequencies, improving output performance. At η=1.341, the output power reaches peaks of 189.72 μW (theoretically) and 188.75 μW (experimentally), indicating that this dimensionless frequency provides optimal resonance conditions and maximizes the coupling effect between the piezoelectric beam and the sphere system. This comparison between the experimental and theoretical values helps validate the theoretical model.

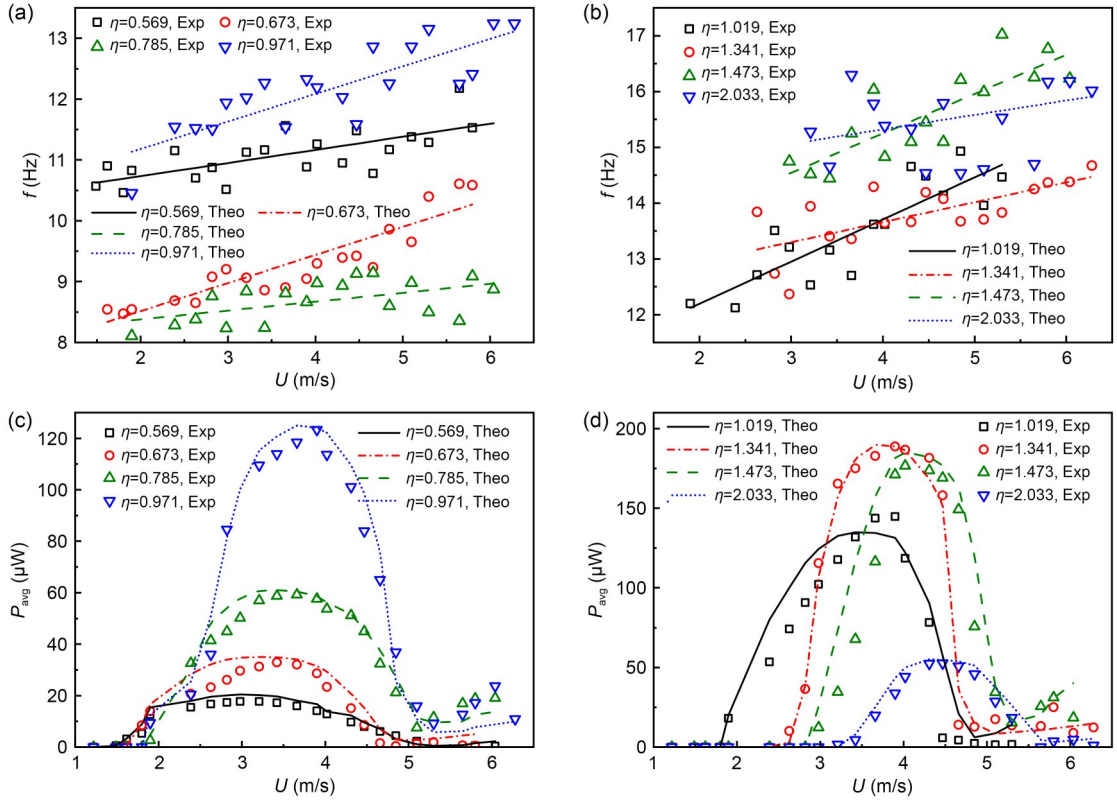

Fig. 6 (a and b) Variation of the vibrational frequency (f) with the wind speed at various dimensionless frequencies (η); (c and d) variation of the average output power (P_{avg}) with wind speed at various dimensionless frequencies (η)

Fig. 7 shows the variation of the aero-electro-mechanical efficiency ψ_{aem} of the proposed energy harvester as a function of load resistance, for different dimensionless frequencies η. $\bar{P}_f$ is the input mechanical power extracted from fluid flow. The formula for aero-electro-mechanical efficiency ψ_{aem} is provided in Section S3 of the ESM. As the resistance R increases from 0.05 to 10.00 MΩ, ψ_{aem} initially increases and then decreases. This occurs because, at low R values, the output voltage is relatively low, reducing the energy harvester's efficiency. However, as load resistance increases to an optimal value, the output voltage reaches its maximum. The peak ψ_{aem} is found at R= 1 MΩ, with a peak value of 1.05%. When $\eta \leqslant 1.34$, increasing the value of η results in a higher ψ_{aem}. However, when η exceeds 1.34, a further increase in η leads to a decrease in ψ_{aem}. This is because an excessively high η value causes the energy harvester's vibration mode to misalign with the fluid flow characteristics, reducing the energy conversion efficiency.

We next show variation curves of the electro-mechanical efficiency (ψ_{em}) of the designed energy harvester with respect to the load resistance at different dimensionless frequencies, as presented in Fig. 8. $\bar{P}_m$ is the average mechanical power. The expression for the ψ_{em} is given in Section S3. Notably, the trends for ψ_{em} and ψ_{aem} are similar, both peaking at R=1 MΩ. This is because the resistance value aligns with the dynamic characteristics of the structure, thereby optimizing the energy conversion efficiency. However, ψ_{em} exhibits significantly higher values, with a peak reaching 28.4%. This indicates that the process of converting mechanical energy from the piezoelectric beam into electrical energy is more efficient than the process of converting fluid energy into electrical energy. ψ_{em} is a measure of the efficiency of converting piezoelectric vibrations into electrical energy, and it tends to have a higher value since it only considers the electro-mechanical conversion step. On the other hand, ψ_{aem} describes the entire energy conversion process, including fluid-driven sphere vibration, sphere-driven piezoelectric beam vibration, and ultimately the conversion of piezoelectric beam vibrations into electrical energy. Consequently, ψ_{aem} might be influenced by energy losses in the earlier stages of the energy conversion process.

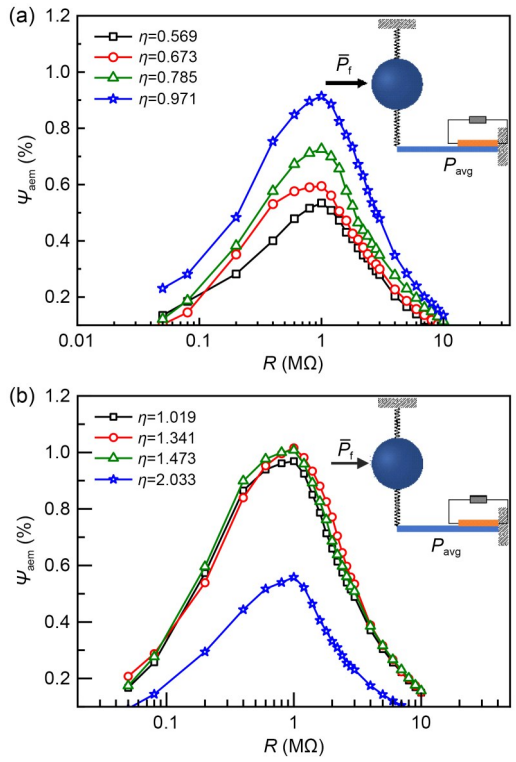

Fig. 7 Variation of the aero-electro-mechanical efficiency (Ψ_{aem}) with load resistance at various dimensionless frequencies: (a) η<1.000; (b) η>1.000

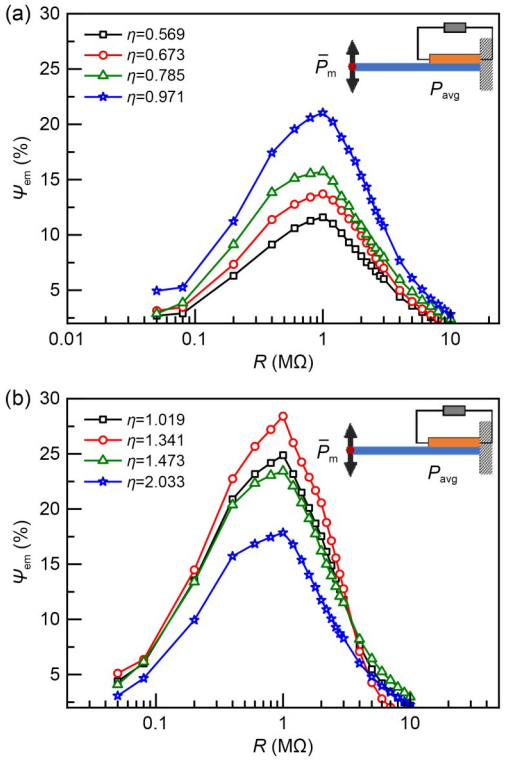

Fig. 8 Variation of the electro-mechanical efficiency (Ψ_{em}) with load resistance at various dimensionless frequencies: (a) η<1.000; (b) η>1.000

4.2 Influence of wind direction on output performance

To investigate the output performance in multiple wind directions, the inflow angle (θ) of the device is adjusted by an indexing dial in the experiment. With the base of the sample mounted on an indexing plate, the direction of the device with respect to the flow can be controlled by an indexing dial. When the inflow direction aligns with the line connecting the sphere and the support column, the angle θ is considered as 0°. Changing the angle θ indicates a change in the inflow direction.

The open-circuit voltage V_{oc} and average output power P_{avg} are recorded at various angles. Figs. 9a and 9c show how the V_{oc} and P_{avg} vary with wind direction at three typical wind speeds. The results were recorded at 12 evenly-spaced angles increasing in a 30° interval. The figures reveal that both V_{oc} and P_{avg} exhibit 180° symmetry, indicating that the energy harvester has strong adaptability to different wind directions. It is only in the range of $150°\leqslant\theta\leqslant210°$ that there is a significant drop in output performance. When the θ is between 150° and 210°, the sphere is positioned behind the support column. The support column obstructs the airflow toward the sphere, causing a change in the airflow pattern around the sphere. This alteration affects the relationship between the lift and drag forces, reducing the vortex force acting on the sphere. As a result, the vibration mode of the sphere changes from vertical to horizontal. When the sphere's vibration mode becomes horizontal, the piezoelectric beam cannot bend, and thus the piezoelectric effect cannot occur, leading to a decrease in energy conversion efficiency. Figs. 9b and 9d show the time history curves of the V_{oc} and P_{avg} for different wind directions, at a wind speed of U=3.90 m/s. When $0°\leqslant\theta\leqslant120°$ and $240°\leqslant\theta\leqslant360°$, the V_{oc} and P_{avg} fluctuate by no more than 5.5%, indicating that the energy harvesting performance is relatively stable across different wind directions. For example, the open-circuit voltage is 36.8 V at θ=0° and 4.9 V at θ=300°, a difference of only 5.1%.

5 Conclusions

A novel piezoelectric energy harvesting device was proposed, which utilizes VIVs of a sphere coupled with a piezoelectric beam to capture wind energy

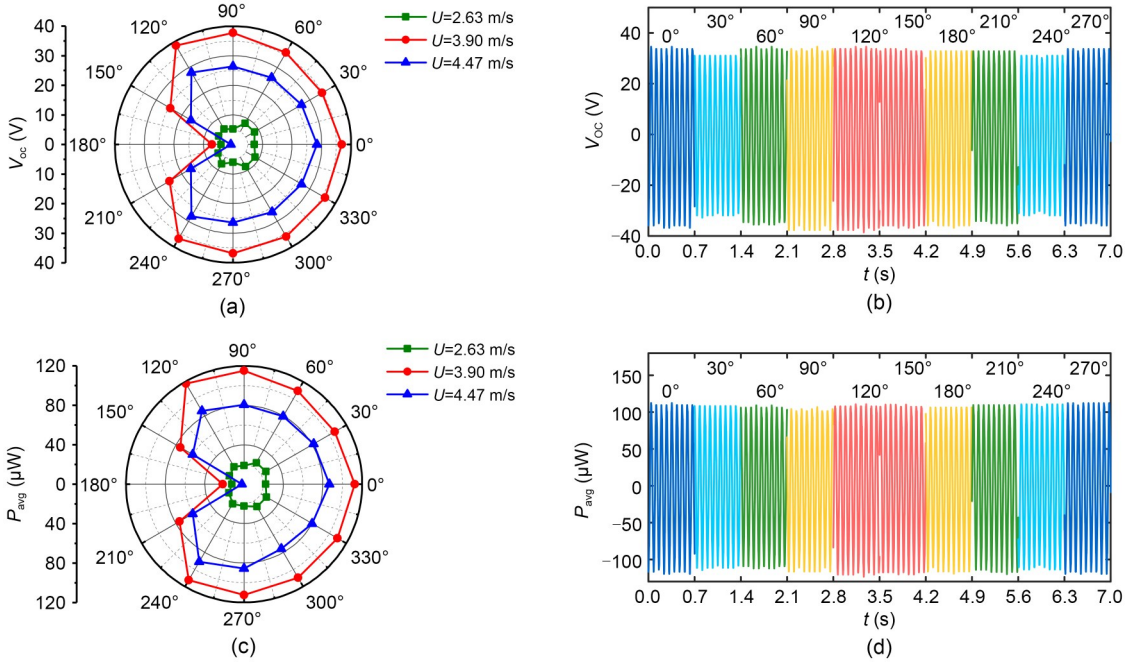

Fig. 9 (a) Variation of the output open-circuit voltage with inflow angle θ at three representative wind speeds; (b) time history curves of peak open-circuit voltage of various angles at U=3.90 m/s; (c) variation of the average output power with inflow angle θ at three representative wind speeds; (d) time history curves of the average output power of various angles at U=3.90 m/s

from varying directions. First, a coupled dynamic theoretical model describing the vibration behaviors and the electrical performance of the energy harvester was developed. The impact of the frequency ratio between the elastic-supported sphere and the piezoelectric beam on the electrical power and lock-in region was investigated, revealing the coupled effect between the sphere and beam oscillations. Moreover, experimental results showed that this new piezoelectric device can harvest wind energy from multiple incoming flow directions.

The fluid forces acting on the sphere to produce VIV behavior were determined through a wake oscillator model. Then, a coupled dynamic model was constructed to analyze vibration responses and interactions between the sphere and the piezoelectric beam. These models were validated by experimental results. Our theoretical and experimental results indicated that the frequency ratio between the sphere and the piezoelectric beam has a strong impact on the electrical performance of the energy harvester. When the frequency ratio was 1.34, the average output power reached a peak of 190 μW at a wind speed of 3.9 m/s. Additionally, the output voltage of the energy harvester was consistent across varying wind speeds and flow directions. This was especially true in the lock-in region, where the peak output voltage varied by less than 5.5%.

Acknowledgments

This work is supported by the National Key R&D Program of China (No. 2021YFF0501001), the National Natural Science Foundation of China (Nos. 52308315, 51922046, and 52192661), the Research Funds of Huazhong University of Science and Technology (No. 2023JCYJ014), the China Postdoctoral Science Foundation (No. 2023M731206), the Research Funds of China Railway Siyuan Survey and Design Group Co., Ltd. (Nos. KY2023014S, KY2023126S, 2021K085, 2020K006, and 2020K172), the Research Fund of China Construction Science and Industry (No. CSCEC-PT-004-2022-KT-3.3), and the Autonomous Innovation Fund of Hubei Province (No. 5003242027), China.

Author contributions

Shun WENG contributed to the methodology, software development, and validation. Liying WU contributed to the methodology, software development and validation, corresponding data processing, and manuscript organization. Lanbin ZHANG contributed to the methodology, experimental design, and software development. Ke GAO, Junshu ZHANG, and Zhiyue ZHANG assisted in organizing the manuscript. Huliang DAI designed and coordinated the manuscript.

Conflict of interest

Shun WENG, Liying WU, Lanbin ZHANG, Ke GAO, Junshu ZHANG, Zhiyue ZHANG, and Huliang DAI declare that they have no conflict of interest.

References

Behara S, Sotiropoulos F, 2016. Vortex-induced vibrations of an elastically mounted sphere: the effects of Reynolds number and reduced velocity. *Journal of Fluids and Structures*, 66:54-68. https://doi.org/10.1016/j.jfluidstructs.2016.07.005

Chen S, Wang CH, Zhao LY, 2023. A two-degree-of-freedom aeroelastic energy harvesting system with coupled vortex-induced-vibration and wake galloping mechanisms. *Applied Physics Letters*, 122(6):063901. https://doi.org/10.1063/5.0128616

Dai HL, Abdelkefi A, Wang L, 2014. Theoretical modeling and nonlinear analysis of piezoelectric energy harvesting from vortex-induced vibrations. *Journal of Intelligent Material Systems and Structures*, 25(14):1861-1874. https://doi.org/10.1177/1045389X14538329

Facchinetti ML, de Langre E, Biolley F, 2004. Coupling of structure and wake oscillators in vortex-induced vibrations. *Journal of Fluids and Structures*, 19(2):123-140. https://doi.org/10.1016/j.jfluidstructs.2003.12.004

Govardhan R, Williamson CHK, 1997. Vortex-induced motions of a tethered sphere. *Journal of Wind Engineering and Industrial Aerodynamics*, 69-71:375-385. https://doi.org/10.1016/S0167-6105(97)00170-0

He LP, Liu L, Zhou JW, et al., 2022. Design and analysis of a double-acting nonlinear wideband piezoelectric energy harvester under plucking and collision. *Energy*, 239:122370. https://doi.org/10.1016/j.energy.2021.122370

Hu GB, Liang JR, Lan CB, et al., 2020. A twist piezoelectric beam for multi-directional energy harvesting. *Smart Materials and Structures*, 29(11):11LT01. https://doi.org/10.1088/1361-665X/abb648

Huang DM, Han JL, Li W, et al., 2023. Responses, optimization and prediction of energy harvesters under galloping and base excitations. *Communications in Nonlinear Science and Numerical Simulation*, 119:107086. https://doi.org/10.1016/j.cnsns.2023.107086

Huang SF, Luo WH, Zhu ZM, et al., 2023. Experimental and theoretical analysis of a hybrid vibration energy harvester with integrated piezoelectric and electromagnetic interaction. *Journal of Zhejiang University-SCIENCE A (Applied Physics & Engineering)*, 24(11):991-1002. https://doi.org/10.1631/jzus.A2200551

Jia JD, Shan XB, Upadrashta D, et al., 2020. An asymmetric bending-torsional piezoelectric energy harvester at low wind speed. *Energy*, 198:117287. https://doi.org/10.1016/j.energy.2020.117287

Machado LQ, Yurchenko D, Wang JL, et al., 2021. Multi-dimensional constrained energy optimization of a piezoelectric harvester for E-gadgets. *iScience*, 24(7):102749. https://doi.org/10.1016/j.isci.2021.102749

Negri M, Mirauda D, Malavasi S, 2018. VIV trajectories of

an elastically mounted sphere. *Applied Ocean Research*, 70:62-75. https://doi.org/10.1016/j.apor.2017.11.006

Rajamuni MM, Thompson MC, Hourigan K, 2018. Vortex-induced vibration of a transversely rotating sphere. *Journal of Fluid Mechanics*, 847:786-820. https://doi.org/10.1017/jfm.2018.309

Rajamuni MM, Thompson MC, Hourigan K, 2019. Vortex-induced vibration of elastically-mounted spheres: a comparison of the response of three degrees of freedom and one degree of freedom systems. *Journal of Fluids and Structures*, 89:142-155. https://doi.org/10.1016/j.jfluidstructs.2019.02.005

Rajamuni MM, Thompson MC, Hourigan K, 2020. Vortex dynamics and vibration modes of a tethered sphere. *Journal of Fluid Mechanics*, 885:A10. https://doi.org/10.1017/jfm.2019.928

Raza SA, Chern MJ, Susanto H, et al., 2020. Numerical investigation of the effects of a small fixed sphere in tandem arrangement on VIV of a sphere. *Journal of Wind Engineering and Industrial Aerodynamics*, 206:104368. https://doi.org/10.1016/j.jweia.2020.104368

Sareen A, Zhao J, Lo Jacono D, et al., 2018. Vortex-induced vibration of a rotating sphere. *Journal of Fluid Mechanics*, 837:258-292. https://doi.org/10.1017/jfm.2017.847

Su C, Gao X, Liu KJ, et al., 2023. Recent advances of ionic liquids in zinc ion batteries: a bibliometric analysis. *Green Energy and Intelligent Transportation*, 2(5):100126. https://doi.org/10.1016/j.geits.2023.100126

Tao JL, Hu J, 2016. Energy harvesting from pavement via polyvinylidene fluoride: hybrid piezo-pyroelectric effects. *Journal of Zhejiang University-SCIENCE A (Applied Physics & Engineering)*, 17(7):502-511. https://doi.org/10.1631/jzus.A1600166

Wang JL, Hu GB, Su Z, et al., 2019. A cross-coupled dual-beam for multi-directional energy harvesting from vortex induced vibrations. *Smart Materials and Structures*, 28(12):12LT02. https://doi.org/10.1088/1361-665X/ab5249

Wang JL, Geng LF, Ding L, et al., 2020. The state-of-the-art review on energy harvesting from flow-induced vibrations. *Applied Energy*, 267:114902. https://doi.org/10.1016/j.apenergy.2020.114902

Wang JL, Yurchenko D, Hu GB, et al., 2021a. Perspectives in flow-induced vibration energy harvesting. *Applied Physics Letters*, 119(10):100502. https://doi.org/10.1063/5.0063488

Wang JL, Sun SK, Tang LH, et al., 2021b. On the use of metasurface for vortex-induced vibration suppression or energy harvesting. *Energy Conversion and Management*, 235:113991. https://doi.org/10.1016/j.enconman.2021.113991

Wang JL, Wang YQ, Hu GB, 2022. Investigation of hybridized bluff bodies for flow-induced vibration energy harvesting. *Journal of Physics D: Applied Physics*, 55(48):484001. https://doi.org/10.1088/1361-6463/ac928e

Williamson CHK, Govardhan R, 1997. Dynamics and forcing of a tethered sphere in a fluid flow. *Journal of Fluids and Structures*, 11(3):293-305. https://doi.org/10.1006/jfls.1996.0078

Wu N, Bao B, Wang Q, 2021. Review on engineering structural designs for efficient piezoelectric energy harvesting to obtain high power output. *Engineering Structures*, 235:112068. https://doi.org/10.1016/j.engstruct.2021.112068

Wu ZH, Xu QS, 2022. Design of a structure-based bistable piezoelectric energy harvester for scavenging vibration energy in gravity direction. *Mechanical Systems and Signal Processing*, 162:108043. https://doi.org/10.1016/j.ymssp.2021.108043

Xia GH, Zhang S, Kang XF, et al., 2023. Performance analysis of nonlinear piezoelectric energy harvesting system under bidirectional excitations. *Composite Structures*, 324:117529. https://doi.org/10.1016/j.compstruct.2023.117529

Xie YL, Li BB, Guo J, 2020. Bayesian operational modal analysis of a long-span cable-stayed sea-crossing bridge. *Journal of Zhejiang University-SCIENCE A (Applied Physics & Engineering)*, 21(7):553-564. https://doi.org/10.1631/jzus.A1900511

Zhang LB, Abdelkefi A, Dai HL, et al., 2017. Design and experimental analysis of broadband energy harvesting from vortex-induced vibrations. *Journal of Sound and Vibration*, 408:210-219. https://doi.org/10.1016/j.jsv.2017.07.029

Zhang LB, Dai HL, Abdelkefi A, et al., 2019. Experimental investigation of aerodynamic energy harvester with different interference cylinder cross-sections. *Energy*, 167:970-981. https://doi.org/10.1016/j.energy.2018.11.059

Zhou LR, Chen L, Xia Y, et al., 2020. Temperature-induced structural static responses of a long-span steel box girder suspension bridge. *Journal of Zhejiang University-SCIENCE A (Applied Physics & Engineering)*, 21(7):580-592. https://doi.org/10.1631/jzus.A1900490

Electronic supplementary materials

Sections S1–S3, Figs. S1–S3